# Analysis of structural and functional aging of electrodes in lithium-ion batteries during rapid charge and discharge rates using synchrotron tomography

Benedikt Prifling[a,*], Alexander Ridder[b], André Hilger[c], Markus Osenberg[d], Ingo Manke[c], Kai Peter Birke[b], Volker Schmidt[a]

[a]*Institute of Stochastics, Ulm University, 89069 Ulm, Germany*
[b]*Electrical Energy Storage Systems, Institute for Photovoltaics, University of Stuttgart, 70569 Stuttgart, Germany*
[c]*Institute of Applied Materials, Helmholtz-Zentrum Berlin für Materialien und Energie GmbH, 14109 Berlin, Germany*
[d]*Department of Materials Science and Technology, Technische Universität Berlin, 10623 Berlin, Germany*

**Abstract**

Predicting and increasing the expected battery lifetime is one of the major objectives in state-of-the-art battery research. Until now, the highly complex mechanisms taking place during cyclic aging are only understood to a certain extent. In the present paper, pristine and cyclically aged battery electrodes are considered and the relationship between their microstructure and functionality is investigated. For this purpose, three-dimensional image data obtained by synchrotron tomography is preprocessed by a novel data-driven trinarization approach based on $k$-means clustering. This allows us to explicitly distinguish between active material, pore space and the phase consisting of binder and conductive additives. This three-phase reconstruction is completed by a segmentation of active material particles, which enables a comprehensive statistical analysis of the electrode morphology. In addition, the investigation of numerous image characteristics together with electrochemical measurements contributes to a deeper understanding of the underlying aging mechanisms.

*Keywords:* Cyclic aging, Lithium-ion batteries, Synchrotron tomography, Trinarization, Particle segmentation, Statistical image analysis

*Corresponding author. Email: benedikt.prifling@uni-ulm.de Phone: +49 731 50 23555, Fax: +49 731 50 23649

## 1. Introduction

In the last few decades, lithium-ion batteries have received a lot of attention due to their superior energy density in combination with decent power density compared to other electrical energy storage systems [1]. Thus, lithium ion batteries are considered as one of the most promising technologies for storing electrical energy. As a consequence, the wide spectrum of applications ranging from portable devices to electric vehicles has led to an ongoing increase in production and therefore a fast-growing demand for raw materials, whose supply can not be guaranteed in the long term. Especially, lithium and cobalt resources will be depleted relatively soon without a proper recycling strategy [2, 3]. Resource consumption could be reduced significantly by improving the aging stability of electrodes and thereby increasing the lifespan of batteries. Thus, the development of lithium-ion batteries with optimized functional properties is one main task in state-of-the-art battery research [4, 5, 6, 7, 8]. This task can be basically achieved in two ways. Either by the development of new battery materials with improved properties [9] or by further improving currently used materials via a deeper understanding of aging phenomena [10, 11, 12].

Due to the advanced research status of lithium-ion batteries, the basics of this promising technology are quite well understood, but there are still a lot of knowledge gaps to be filled due to the complex chemical reactions taking place during operation. In particular, the aging mechanisms are not fully understood yet and need to be further investigated since the understanding of aging phenomena is the key to long-lasting batteries for future applications and essential for the development of improved energy storage systems. Of course, there have been made several attempts to better understand the aging mechanisms, e.g., statistical approaches [13, 14] or procedures based on electrochemical characteristics observed in accelerated aging tests [15, 16]. For a comprehensive review of aging mechanisms and different approaches for lifetime prediction of lithium-ion batteries, we refer to [17, 18]. One major problem is that the investigation of the electrode microstructure during aging is difficult. In addition, quantitative studies are complicated due to the small examined volume especially of the solid electrolyte interface (SEI) and the high reactivity of the cell components [19, 20]. Nevertheless, the investigation of pristine and aged electrode microstructures

allows us to gain insight into the processes that take place during aging since the microstructure of anodes as well as cathodes significantly influences the resulting electrochemical performance, see [21, 22] for the influence of size and shape of active particles and [23] for the importance of spatially localized features. For this purpose, a lot of different imaging techniques like X-ray diffraction (XRD), X-ray photoelectron spectroscopy (XPS) and electron spectroscopy (SEM or TEM) can be applied [24, 25, 26]. In the present paper, synchrotron tomography is used to obtain 3D images of pristine and cyclically aged electrodes. By means of a novel trinarization approach, active material, pores and the phase consisting of binder and conductive additives (briefly called ba-phase in the following, sometimes denoted by CBD) are reconstructed from tomographic image data. The proposed procedure allows for a comprehensive structural characterization of the battery electrodes, which can be correlated with functional properties to contribute to a deeper understanding between the electrode morphology and the electrochemical performance.

The rest of this paper is organized as follows. In Section 2, we give a detailed description of the considered commercial anodes and cathodes as well as the cyclic aging process and the tomographic imaging procedure by means of synchrotron tomography, which accounts for spatially-resolved features. Then, in Section 3, the resulting 3D image data is preprocessed using various segmentation algorithms. More precisely, we distinguish between active material, the phase consisting of binder and conductive additives and the pore space by means of a novel data-driven trinarization approach, which classifies each voxel based on local grayscale information. In addition, the image processing includes the segmentation of individual active particles. Using the preprocessed 3D image data, we compute phase-based and particle-based image characteristics in order to detect and quantify the structural changes caused by cyclic aging. In Section 4, we discuss the electrochemical measurements and relate the findings to the results of Section 3. Finally, in Section 5, we conclude the paper with a short summary and discussion of the main results.

## 2. Experimental

In this section, we describe the material composition, the cyclic aging procedure and the imaging process in detail.

### *2.1. Material description*

Commercial electrodes by Custom Cells (Itzehoe, Germany) were used both for anode and cathode. Two batches of high energy graphite electrodes with a composition of 96 wt% active material, 2 wt% conductive additives and 2 wt% binder were used on the anode side. Batch one exhibited a nominal capacity of 3.83 $\mathrm{mAhcm^{-2}}$ (which leads to 9.76 mAh for one electrode) and was coated on an 18 µm thick copper foil. Batch two had a capacity of 3.80 $\mathrm{mAhcm^{-2}}$ (leading to 9.67 mAh total) and was coated on 14 µm copper foil. On the cathode side, two batches with high energy lithium nickel copper manganese oxide ($\mathrm{LiNi_{1/3}Co_{1/3}Mn_{1/3}O_2}$, briefly called NCM in the following) as active material were used. Batch one cathodes consisted of 86 wt% active material, 8 wt% conductive additives and 6 wt% binder, whereas the material composition of batch two is given by 90 wt% active material, 5 wt% conductive additives and 5 wt% binder. Both NCM electrodes were coated on a 20 µm aluminum foil and provided a nominal capacity of 9.01 mAh (batch one) and 8.79 mAh (batch two), respectively.

### *2.2. Cyclic aging*

The pristine electrodes were used as provided by the supplier while the aged electrodes were aged using cell cases ECC-PAT-Core by EL-Cell (Hamburg, Germany) with stainless steel plungers (also EL-Cell) and used polypropylene membranes as separators (Celgard 2500. Celgard, Charlotte, North Carolina, USA) as well as 1M $\mathrm{LiPF_6}$ in 1:1 EC:DEC electrolyte (LP40 by BASF, Ludwigsburg, Germany). Cycling is carried out at room temperature with a ACT0550 battery cell tester from PEC (Leuven, Belgium).

To achieve a rapid aging of the electrodes leading to more pronounced structural changes, very high C-rates were chosen. To evaluate our method and due to the resolution of the used X-ray CT

method, more pronounced changes in the material are favorable, which are occurring during high C-rates. Additionally this treatment provides information on high rate charging and discharging which is one extreme a cell might experience in her lifetime for example in a hybrid electronic vehicle [27, 28]. The cells underwent a formation with two C/10 and two C/5 cycles. The actual aging was carried out with a 2C ($= 6.92\,\mathrm{mAcm^{-2}}$) charge followed by a CV-phase, which was limited to 20 minutes or a minimal current of C/10. Discharge was done with 4C ($= 13.84\,\mathrm{mAcm^{-2}}$). Note that all C-rates were nominated on the theoretical capacity of the batch one NCM electrodes, which is given by 8.79 mAh.

### *2.3. Sample preparation and imaging procedure*

After cycling the cells were disassembled under argon atmosphere and the electrodes were washed with dimethylcarbonate to remove remaining electrolyte and prevent further reactions. The graphite electrodes were gently removed from the copper current collector with a scalpel and a piece with a size of approximately $2 \times 2 \times 2\,\mathrm{mm^3}$ was cut out. With regard to the NCM electrodes, the current collector was not removed as aluminum is light enough not to hinder the tomographic imaging procedure.

The synchrotron tomography measurements have been conducted at the imaging beamline (IBL) P05 which is operated by the Helmholtz-Zentrum Geesthacht (HZG) at the PETRA III storage ring (DESY) [29, 30]. The synchrotron beam was generated with an undulator (2 m in length) and monochromatized with a double crystal monochromator to an energy of 31 keV with energy resolution of $\frac{\Delta E}{E} \approx 10^{-4}$. After transmitting the sample, the monochromatic X-rays were transformed into visible light with a $CdWO_4$ scintillator. The optical set-up provided a 20 times magnification and the image was detected with an EHD SC09000M CCD camera with $3056 \times 3056$ pixels. A $1.8 \times 1.8\,\mathrm{mm^2}$ field of view was captured with a pixel size of 0.574 µm. For each tomography, 1200 radiograms over an angular range of 180° were captured with an exposure time of 1 s. For the data processing and reconstruction Matlab based routines were used. The tomographic reconstruction

was performed with the ASTRA toolbox [31, 32]. The voxel size of the reconstructed 3D image data equals 1.148 µm.

Altogether, two graphite electrodes (one pristine and one cyclically aged sample) as well as five NCM electrodes (two pristine and three cyclically aged samples) were measured. Additional information regarding the samples can be found in Table 1.

| sample number | 1 | 2 | 3 | 4 | 5 | 6 | 7 |
|---|---|---|---|---|---|---|---|
| electrode | cathode | cathode | cathode | cathode | cathode | anode | anode |
| cyclically aged | no | yes | yes | no | yes | no | yes |
| batch | 1 | 1 | 1 | 2 | 2 | 2 | 2 |
| number of cutouts | 10 | 10 | 10 | 10 | 10 | 9 | 10 |

Table 1: General sample information.

## 3. Image processing and image analysis

This section deals with processing and statistical analysis of the 3D tomographic image data described in Section 2.3.

### *3.1. Image preprocessing*

In order to compute microstructural characteristics, the tomographic image data had to be appropriately preprocessed. At first, a non-local means filter for denoising the reconstructed images with a local neighborhood size of one and a search volume size of $11^3$ voxels has been applied in order to smooth the images while preserving edges [33, 34]. Next, the samples have been straightened using polynomial regression. In order to increase the explanatory power of shape characteristics, which will be discussed later, the resolution has been doubled by using trilinear interpolation, leading to a voxel size of $0.574 \times 0.574 \times 0.574\,\mu m^3$ [35].

*3.1.1. Phase-based segmentation*

The next step is to obtain a reasonable phase-based segmentation, i.e., we want to distinguish between the active material phase (am-phase), the pores and the phase consisting of binder and conductive additives (ba-phase). In order to realistically describe the morphology of electrodes it is crucial to explicitly distinguish between pores and the ba-phase since the morphology of the ba-phase influences the performance of anodes [36, 37] and cathodes [38, 39]. Typically, in the literature, the three phases mentioned above are reconstructed from FIB/SEM images since this imaging technique provides a comparatively high contrast [40, 41, 42]. However, one of the disadvantages of this imaging method is that the measured volume is rather small leading to the possible danger of considering a volume element that is not representative. In contrast to this, the imaged volume is significantly larger when using X-ray imaging techniques as for example synchrotron tomography. In this context, the segmentation of phases is frequently restricted to the reconstruction of active material and non-active material due to the low contrast between the ba-phase and the pore space [43, 44, 45, 46, 47]. In recent years, several approaches have been developed to include the morphology of the ba-phase based on the reconstruction of the active particles, e.g., using a morphological closing [48] or stochastic methods [49]. In [50], it has been shown that modeling the ba-phase by a coating (also called dilation) of active particles does not mimic the distribution of the ba-phase realistically, whereas the presence of binder and conductive additives near particle contacts is more suitable. Since it is not possible to distinguish between pores and the ba-phase by direct visual inspection, in the present paper, we apply a data-driven segmentation approach that basically consists of three steps. The first step is the decomposition of the grayvalue histogram into three parts, where each part corresponds to one phase. Afterwards, we apply the method of $k$-means clustering using $k = 3$ clusters [51]. The third step can be considered as post-processing which corrects some minor problems of the $k$-means algorithm. These three steps are applied to all samples described in Table 1 and will be explained in detail in the following. The plots in Figure 1 are based on the pristine anode, which is used to visualize the trinarization approach exemplarily.

At first glance, the histogram of grayvalues does not exhibit three clearly visible peaks, see Figure 1a. This might seem quite counterintuitive since we would expect to observe three peaks in the histogram, each of them corresponding to one phase. Since the locations of the peaks are in general not given by clearly visible local maxima, we fit a Gaussian mixture model with three components to the data set of observed grayvalues [52]. The fitting itself is done in MATLAB and uses the EM-algorithm with a maximum number of 2000 iterations and a tolerance of $5 \cdot 10^{-6}$. This powerful tool attracted a lot attention since the publication of Dempster, Laird and Rubin [53] and the proof of convergence by Wu in 1983 [54]. In order to ensure that the resulting Gaussian mixture model nicely reflects the observed histogram, we manually set the initial values for mean and standard deviation of the three normal distributions, denoted by $\mu_P, \mu_{BA}, \mu_{AM}, \sigma_P, \sigma_{BA}$ and $\sigma_{AM}$. In addition, the initial guesses for the volume fraction of each phase, denoted by $\xi_P, \xi_{BA}, \xi_{AM} \in [0, 1]$, are preset. The approximation of the grayvalue histogram by a mixture of three normal distributions is visualized in Figure 1b. The symmetric histogram of active material voxels is now "subtracted" from the entire histogram, where the location of the peak of the active material phase is given by $\mu_{AM}$. More precisely, we compute the distribution of grayvalues corresponding to the active material phase by mirroring the grayvalue distribution at the right hind side of $\mu_{AM}$. Analogously, we "subtract" the histogram of all pore voxels, where the location of the corresponding peak is given by $\mu_P$. The final decomposition of the histogram can be seen in Figure 1c.

After having decomposed the histogram into three parts, we use this decomposition as input for the second step. In this step, we partially reconstruct the active material phase by setting all voxels with a grayvalue larger than $\mu_{AM}$ to active material. Analogously, we set all voxels with a grayvalue lower than $\mu_P$ to pore. Next, we iterate over all voxels $v_1, ..., v_n$ with a grayvalue between $\mu_P$ and $\mu_{AM}$ and compute for each voxel $v_i$ the sorted grayvalues of all 124 neighboring voxels ("feature vector" $w_i \in \mathbb{R}^{124}$ ), i.e., the sorted grayvalues of all voxels in the $5 \times 5 \times 5$ window centered at the currently considered voxel. Afterwards, we apply $k$-means clustering with $k = 3$ clusters in order to assign each voxel $v_i$ its corresponding label according to the information stored

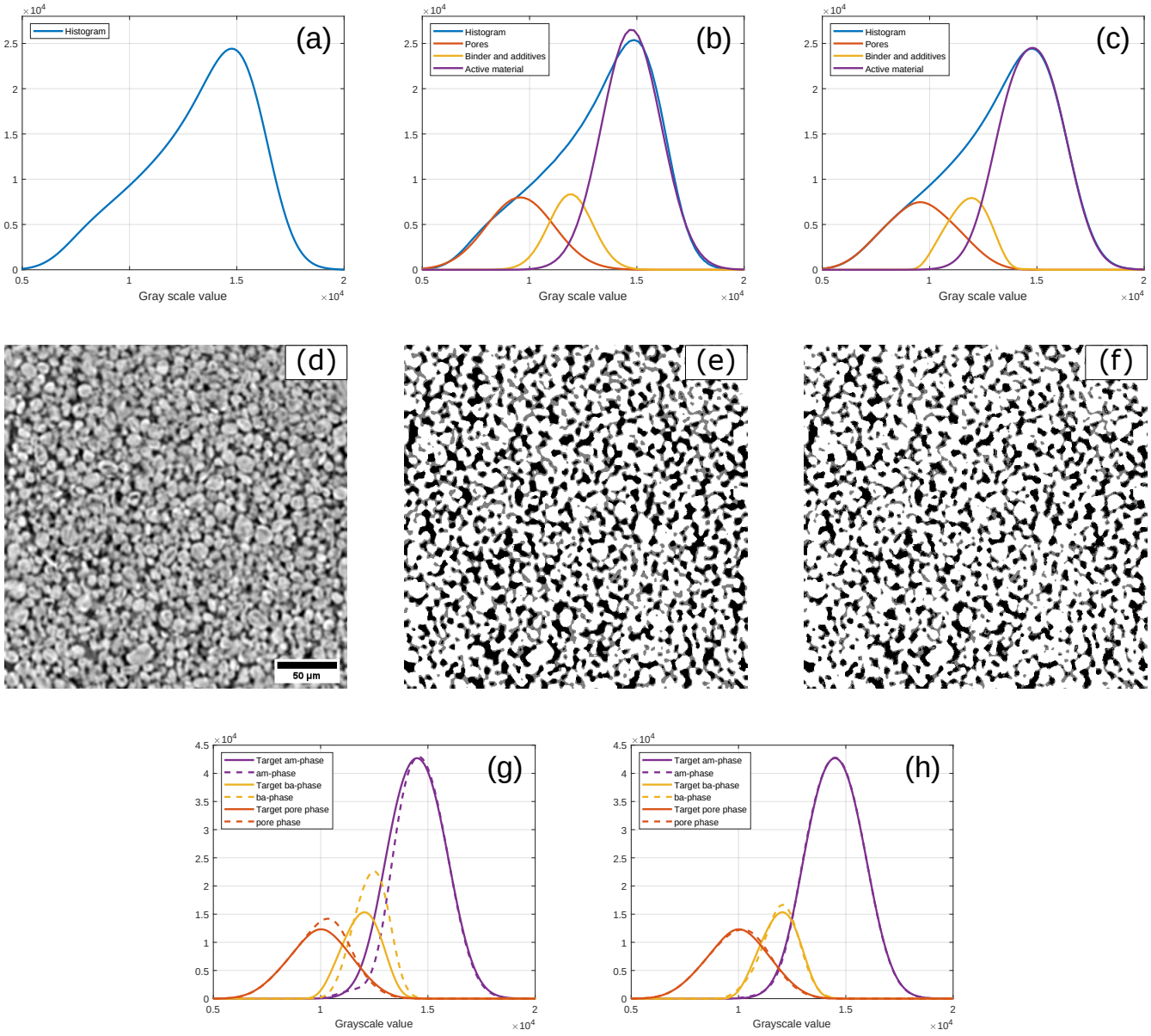


Figure 1: All plots in this figure refer to sample six, i.e., the pristine anode. Histogram of grayvalues (a), decomposition of the histogram by means of a Gaussian mixture model with three components (b) and final decomposition of the histogram (c). Center row: Two-dimensional cutout (287 µm × 287 µm) of the 16-bit grayscale image (d), result of the $k$-means cluster algorithm (e) and final trinarization obtained by applying the post-processing step (f). Bottom row: Comparison of the three histograms obtained by the histogram decomposition (solid lines) and the histograms computed from the trinarization (dashed lines). Result of the $k$-means cluster algorithm (g) and trinarization after applying the post-processing step (h).

in the "feature vectors", see [55]. By doing so, the decision to which cluster a certain voxel belongs is based on the grayvalues in a certain local neighborhood. Since the result of $k$-means clustering depends on the choice of the initial cluster centers [56], we initialize the three cluster centers in the following way. We consider all voxels with a grayvalue in the interval $[\mu_{AM}, \mu_{AM} + 100]$ and compute the averaged "feature vector" $w_{AM}$. The cluster center of active material, denoted by $c_{AM}$, is given by $v_{i_{AM}}$, where $i_{AM} = \underset{j=1,...,n}{\arg\min} \|w_j - w_{AM}\|$ and $\|\cdot\|$ denotes the Manhattan distance, where the Manhattan distance of a vector $x = (x_1, ..., x_d) \in \mathbb{R}^d$ is given by $\|x\| = \sum_{i=1}^{d} |x_i|$. Roughly speaking, $v_{i_{AM}}$ can be regarded as a typical or representative active material voxel. Analogously, we iterate over all voxels with a grayvalue in the interval $[\mu_P - 100, \mu_P]$ and, once again, compute the averaged "feature vector" $w_P$. The cluster center of the pore space is given by $v_{i_P}$, where $i_P = \underset{j=1,...,n}{\arg\min} \|w_j - w_P\|$. Figure 1e shows the result of the $k$-means cluster algorithm in comparison to the underlying gray scale image (Figure 1d). Note that in the present paper, we will use the following colors for visualization: Active material (white), pores (black) and ba-phase (gray). By visual comparison, the phase-based segmentation looks reasonable except for two minor issues. On the one hand, there are very small clusters of active material voxels, where the gray scale image does not indicate active particles. On the other hand, there are small holes inside the active material phase.

To account for these two issues, the third step of the trinarization procedure is a post-processing step, which receives the output of the $k$-means cluster algorithm as input. At first, all holes inside active particles are detected by the Hoshen-Kopelman algorithm [57] and set to the active material phase. Afterwards, a grayscale opening with a ball of radius one as structuring element [58] is performed in order to smooth the microstructure. Due to decomposition of the histogram into three parts, the target volume fractions of all three phases can be computed. This information is incorporated into the post-processing step in the following way. Since it can be observed that the volume fraction of active material is slightly underestimated by the $k$-means algorithm, we itera-

tively add the voxel with the highest number of active material voxels within the 26-neighborhood to the am-phase until the target volume fraction of the am-phase is exactly achieved. At this point, the porosity is typically smaller than the target porosity. Thus, the last part of the post-processing step iteratively assigns the voxel with the highest number of pore voxels within the 26-neighborhood to the pore phase until the target porosity is matched. On the one hand, the post-processing step allows us to achieve the target volume fraction of each phase. On the other hand, this algorithm influences only a relatively small number of voxels such that the main features of the $k$-means clustering result are preserved, see Figure 1f.

The trinarization approach presented above seems to be reasonable if one compares the grayscale image (Figure 1d) with the corresponding trinarization (Figure 1f), i.e., the phase-based segmentation classifies voxels as active material, which one would also have classified as active material by visual inspection. In addition, the trinarization procedure can be validated by comparing the histogram decomposition with the histogram, which is computed from the trinarization. From Figure 1g, it can be seen that the result of the $k$-means algorithm is mostly meaningful. Figure 1h shows that the post-processing step is able to further improve the goodness of fit. Since the size of binder and conductive additives is smaller than the resolution of the 3D image data, we consider a voxel belonging to the ba-phase as nanoporous voxel. More precisely, such a voxel only consists of binder and conductive additives to a certain extent, where different values for the nanoporosity are reported in the literature. More precisely, a nanoporosity of 47% is reported in [59], whereas the values of 28% and 58% can be found in [60] and [61], respectively.

#### *3.1.2. Particle-based segmentation*

In order to investigate the system of active particles, a particle-based segmentation of the am-phase is performed by means of a marker-based watershed algorithm [62]. At first, the regional minima of the negative Euclidean distance transform of the am-phase image are computed. In a next step,

we consider the parameter $\varepsilon > 0$ allowing us to extend these minima, which serve as markers for the marker-based watershed algorithm [63]. More precisely, a regional minimum additionally includes those neighboring voxels whose values in the negative Euclidean distance transform do not differ by more than $\varepsilon$ from the value of the regional minimum. Due to the extension of regional minima, the number of markers and thus the number of particles is reduced, which partially reduces over-segmentation. After the flooding process, the labelled 3D image is used as input for a final post-processing step, which involves the parameter $r > 0$ [64]. Mathematically speaking, we iterate over all particles and successively dilate each particle $P_i$ using a ball of radius $r$ as structuring element. If the dilated particle completely covers another (undilated) particle $P_j$, the marker of $P_j$ is removed. If the reverse case holds too (i.e., the dilated particle $P_j$ completely covers $P_i$), the marker of the smaller particle is eliminated. By a careful choice of both parameters $\varepsilon$ and $r$ (see Table 2) one is able to significantly reduce over-segmentation and thus to provide a meaningful particle-based segmentation of the active particles as it can be seen in Figure 2. For a comprehensive overview of the field of mathematical morphology, the reader is referred, e.g., to [58] and [65].

| sample number | 1 | 2 | 3 | 4 | 5 | 6 | 7 |
|---|---|---|---|---|---|---|---|
| $\varepsilon$ | 1.5 | 1.25 | 1.25 | 1.5 | 1.5 | 0.9 | 0.9 |
| $r$ | 6.0 | 5.0 | 6.0 | 6.0 | 6.0 | 4.5 | 4.5 |

Table 2: Parameter values influencing the particle-based segmentation.

### *3.2. Image analysis*

This section covers the microstructural analysis of the preprocessed tomographic image data. All results are averaged over several cutouts of size 287 µm × 287 µm with respect to the in-plane direction. The corresponding size in through-plane direction has been chosen such that no void space is contained in the cutout in order to avoid edge effects. The number of cutouts for each sample can be found in Table 1.

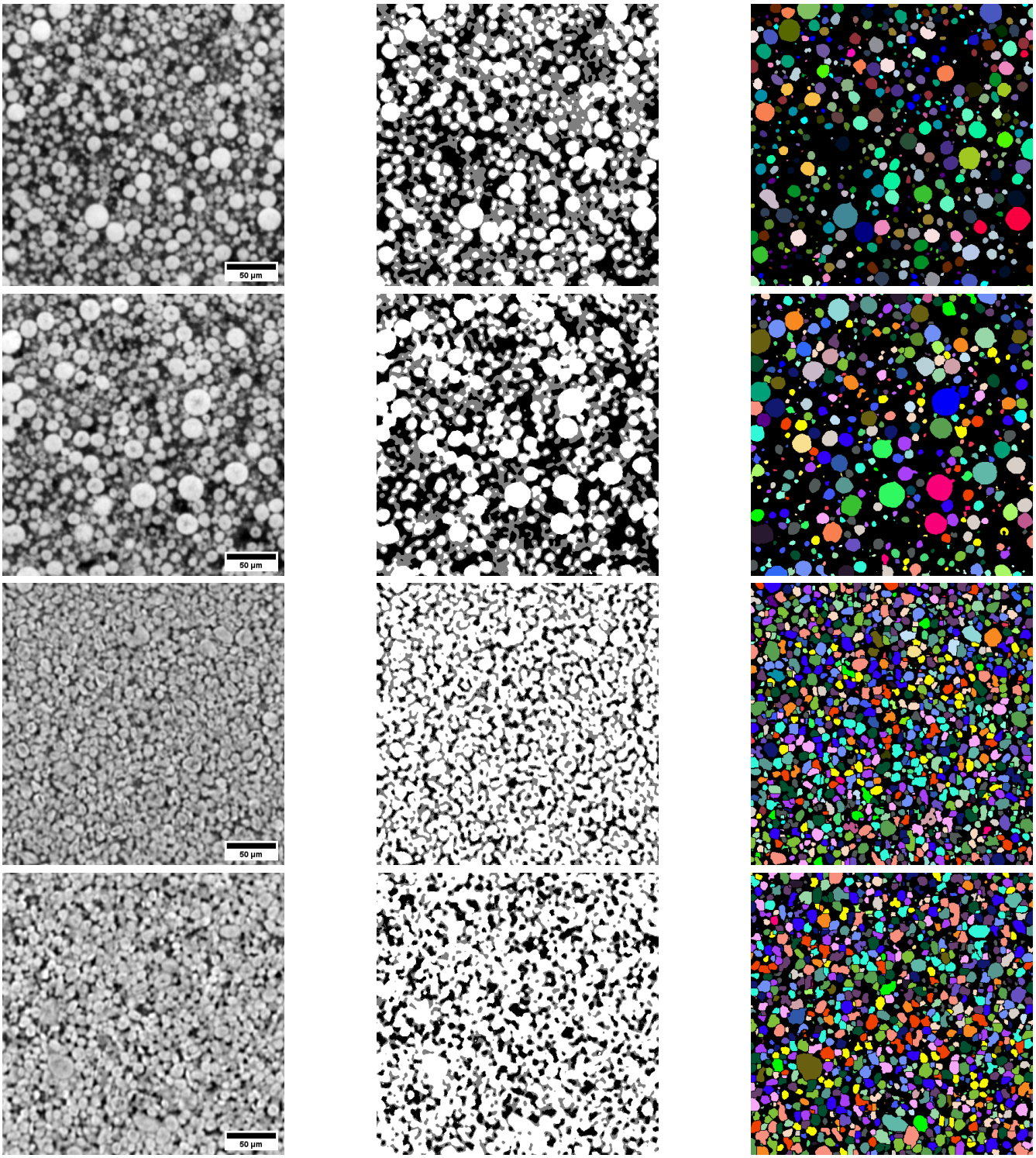


Figure 2: Two-dimensional in-plane cutouts (287 µm × 287 µm) of the 16-bit grayscale image (left), the corresponding trinarization (center) and the particle-based segmentation (right). The corresponding samples are (from top to bottom): Pristine cathode (sample four), cyclically aged cathode (sample five), pristine anode (sample six) and cyclically aged anode (sample seven).

*3.2.1. Phase-based image characteristics*

In this section, we deal with phase-based image characteristics, i.e., we make use of the three-phase reconstruction described in Section 3.1.1. to quantitatively characterize the morphology of the am-phase, the ba-phase and the pore space.

To begin with, we focus on the volume fractions of each phase, which are shown in Figure 3a. Note that the values for sample 5 sum up to 99.9 percent because of rounding errors. Keep in mind that the ba-phase exhibits nanopores leading to a potential underestimation of porosity. In addition, it is not clear whether the nanoporosity is affected by cyclic aging. The volume fraction of the active material as well as the porosity increase during cyclic aging for both batches of cathodes. The increasing volume fraction of active material of cyclically aged cathodes compared to the pristine samples is also reported in [64] and might be caused by the partly irreversible volume changes during charge and discharge of NCM. With regard to both cathode batches, the volume fraction of the ba-phase is getting smaller by a considerable amount. This can at least partly be explained by the compression of the ba-phase during assembly and operation, as it is the softest and most flexible part of the electrode. Note that we can observe large differences between sample two and three in spite of the fact that both samples are cyclically aged batch one cathodes. This suggests that the complex aging mechanisms strongly depend on small spatially localized features. In addition, we have observed a contrary behavior of anodes compared to cathodes, which has also been reported in [66]. Furthermore, the microstructural changes with respect to the anodes are less pronounced compared to the cathodes.

Next, we consider the specific surface area (SSA) of each phase. This quantity is computed by dividing the surface area of the considered phase by the volume of the sampling window. To compute the surface area we use an algorithm proposed in [67], which is based on local $2 \times 2 \times 2$ voxel configurations with different weights. The results are visualized in Figure 3b. The increased specific surface areas of pores and active material of the cathodes suggest swelling or breaking of

the particles during aging, where the appearance of the latter effect is supported by the increased SSA of the pore phase. An increase of SSA of active material has already been reported in [64]. As the ba-phase is compressed during cycling its SSA is decreasing while the SSA of the pore space is increasing. Considering the anodes, the SSAs of all three phases are decreasing which can be explained by the creation of the SEI and lithium plating on the surface of the graphite particles during aging [66, 68]. When the SEI is formed, pore space near the surface of the particles in the ba-phase is filled as the thickness of the film ranges from several nanometers up to nearly one micrometer [19]. This leads to a decrease in SSA for the am- and ba-phase as well as the pore space. When lithium plating occurs, pores in the same region are filled which leads to an even more extensive decrease in SSA of all three phases. See [69] for more detailed information on lithium plating. Note that the effect of SEI formation on the SSA is negligible when considering the cathode since the SEI thickness in the cathode is so thin that it can not be detected in images obtained by synchrotron tomography.

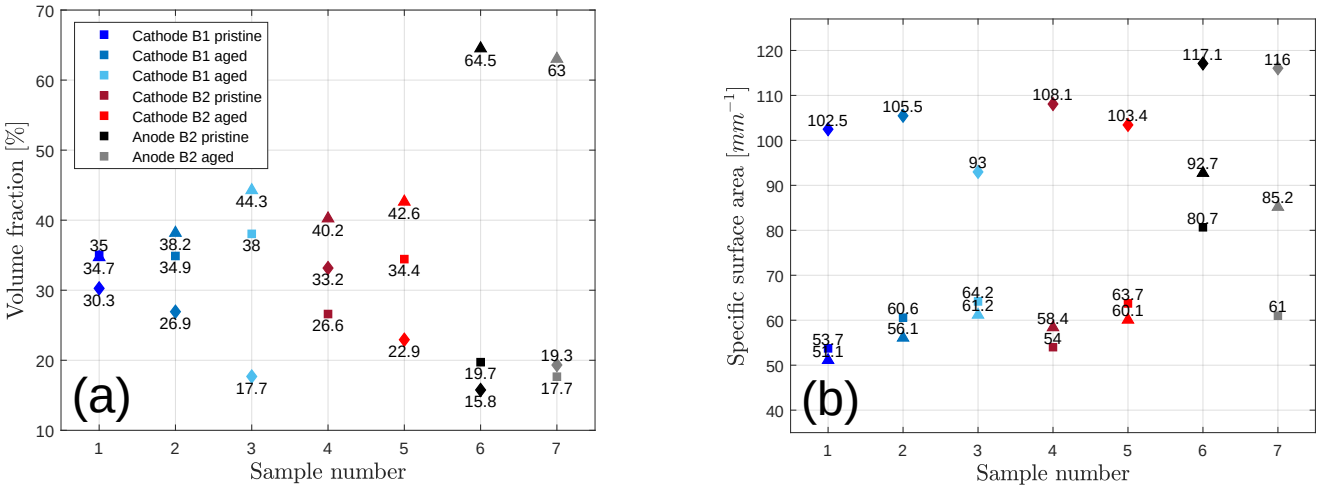


Figure 3: Volume fraction (a) and specific surface area (b) of am-phase (triangles), pores (squares) and ba-phase (diamonds) for each sample. Note that the legend of the plot on the left-hand side is also valid for the plot on the right-hand side.

Another important quantity is the so-called geodesic tortuosity, which is strongly related to trans-

port phenomena in porous media [70]. It is worth mentioning that geodesic tortuosity is a purely geometric characteristic in contrast to several other concepts of tortuosity, see [71, 72]. More precisely, geodesic tortuosity is a direction-dependent characteristic and can be computed with respect to an arbitrary phase. Once a transport direction is chosen, the lengths of shortest paths, which have to be completely contained in the respective phase, from the starting plane to the destination plane are computed using the Dijkstra algorithm [73]. The distribution of geodesic tortuosity is then obtained as the quotients of the shortest paths lengths divided by the thickness of the material. Since ionic and electrical transport mainly take place in through-plane direction, this characteristic is computed in $z$-direction, i.e., from current collector to separator. The results regarding the different phases, i.e., am-phase, ba-phase, pore space and the union set of ba-phase and pore space (called bap-phase in the following), are shown in Figure 4. Note that the fluctuations of the five curves belonging to the cathodes in Figure 4d are caused by the fact that geodesic tortuosity is computed on a discretized image, where the volume fraction of the corresponding phase is rather large. In addition, it can be observed that the length of shortest transport paths in the am-phase, the pore space and the bap-phase do not change significantly due to cyclic aging when considering both cathode batches. With respect to the ba-phase, we can conclude that mean geodesic tortuosity increases during aging, which is likely to be caused by the compression and displacement of this phase due to increasing pressure in the cell. With regard to anodes, the mean lengths of shortest transport paths in the bap-phase, am-phase as well as the pore space are significantly increased during cycling, which indicates that ionic as well as electrical transport is hindered due to the structural changes caused by aging.

This is consistent with the results regarding the specific surface area as its decrease can be explained by SEI formation and lithium plating. These phenomena block transport paths in the pore phase which results in longer transport ways [74]. Additionally, the longer pathways in the active material are likely to be caused by particle cracking, which may be one of the main processes causing the aging of the anodes and may not be entirely visible in CT measurements [75]. This may not cause a significant increase in the ionic transport path lengths as the cracks are likely to

be filled in the first place with SEI, which is ionically conductive. In contrast to the active material as well as the pore space, mean geodesic tortuosity of the ba-phase in the anodes does not change significantly, whereas the shape of the distribution is getting more narrow.

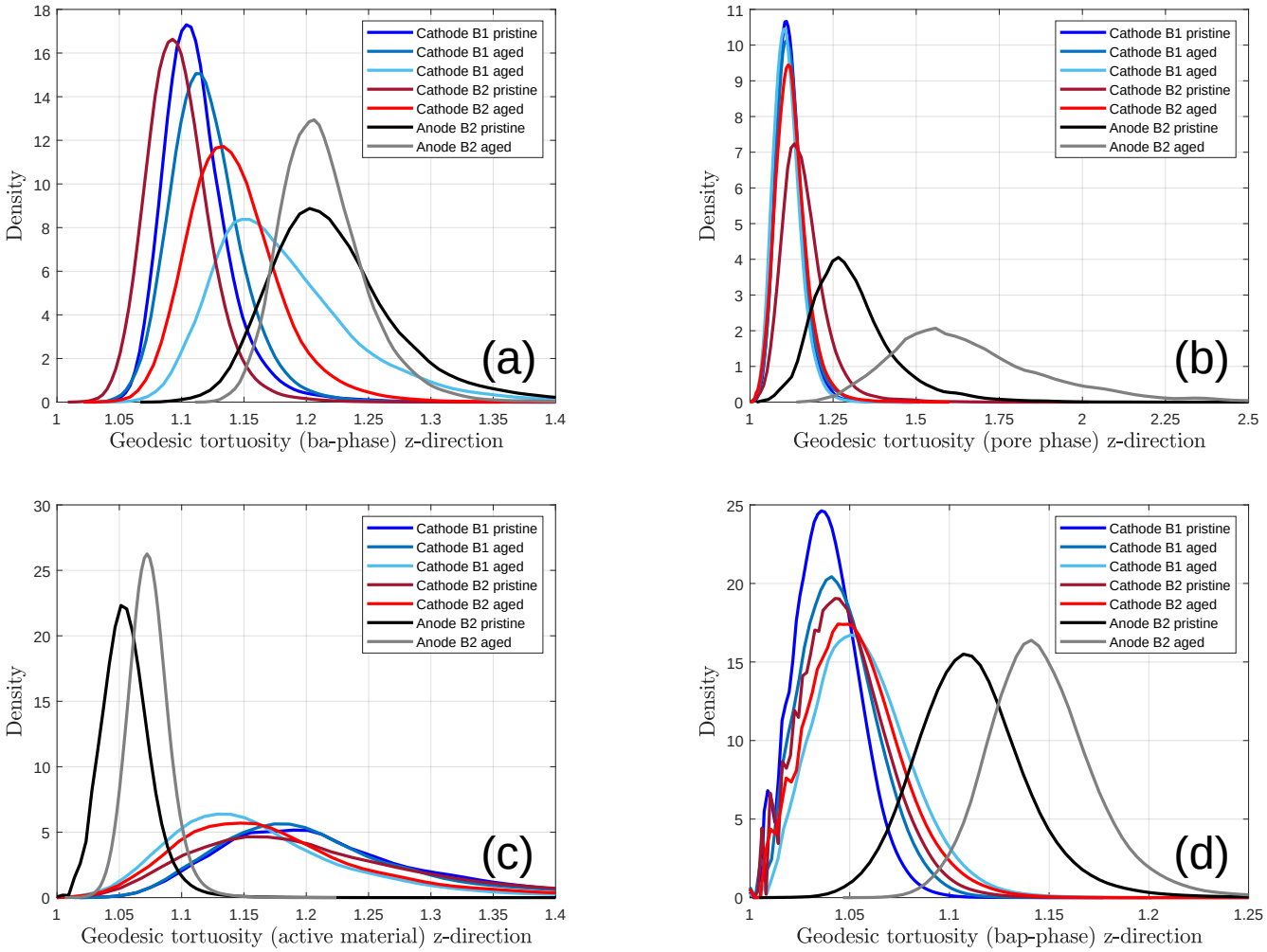


Figure 4: Distribution of geodesic tortuosity of the ba-phase (a), the pore space (b), am-phase (c) and the bap-phase (d) for each sample.

In order to further characterize the 3D morphology of the ba-phase and the pore space, we consider the continuous phase size distribution (CPSD), see [76, 77]. For each radius $r$, we compute the volume of the considered phase, which can be completely filled by balls of radius $r$. The union of

the balls is not allowed to intersect with the complement of the predefined phase. The results are shown in the top row of Figure 5. Considering the cathodes, cyclic aging leads to a shift of CPSD of the ba-phase to the left, i.e., the aged electrodes possess smaller ba-phase components. Once again, there is a remarkable difference between sample two and three (both cyclically aged cathodes from batch one) as it has been already seen with regard to volume fractions. When considering the pore phase, one can observe that the main difference between those two samples is that sample three exhibits more smaller pores whereas sample two possesses a higher portion of larger pores. With regard to batch two cathodes, it can be observed that especially smaller pores are created due to aging. Furthermore, the anodes again show a different behavior compared to cathodes. More precisely, cyclic aging leads to a significant decrease of small pores. With respect to the ba-phase, we detect a uniform increase of the obtained values. These changes can be explained by SEI growth and lithium plating, which occur on top of the particle surface and block especially the smaller pores. Notably the resulting lithium layer is rather invisible for X-ray CT method as it provides very low absorption and can only be seen with phase contrast methods [78].

In a next step, we analyzed the results of simulated mercury intrusion porosimetry (MIP), see [76]. In contrast to the CPSD, the results of MIP are direction-dependent. In the present paper, the direction of interest is from separator to current collector ($z$-direction) since ionic and electrical transport phenomena mainly take place in this direction. The only difference compared to CPSD considered above is that the balls of radius $r$ are no longer allowed to be arbitrarily placed within the considered phase. Instead, they have to form an intrusion along the predefined direction. The results regarding this characteristic are shown in bottom row of Figure 5. Of course, the curves tend to drop faster since MIP accounts for bottlenecks. Apart from that, the curves show a very similar behavior compared to those of CPSD with respect to the ba-phase as well as the pore space. Once again, the changes on the anode side can be explained with additional SEI formation and lithium plating, where lithium plating leads to limited ionic transport but higher electrical conductivity as less pores block the transport of electrons. At the same time the surface area for the phase transition into the particles is getting harder to reach which could result in an all-in-all less

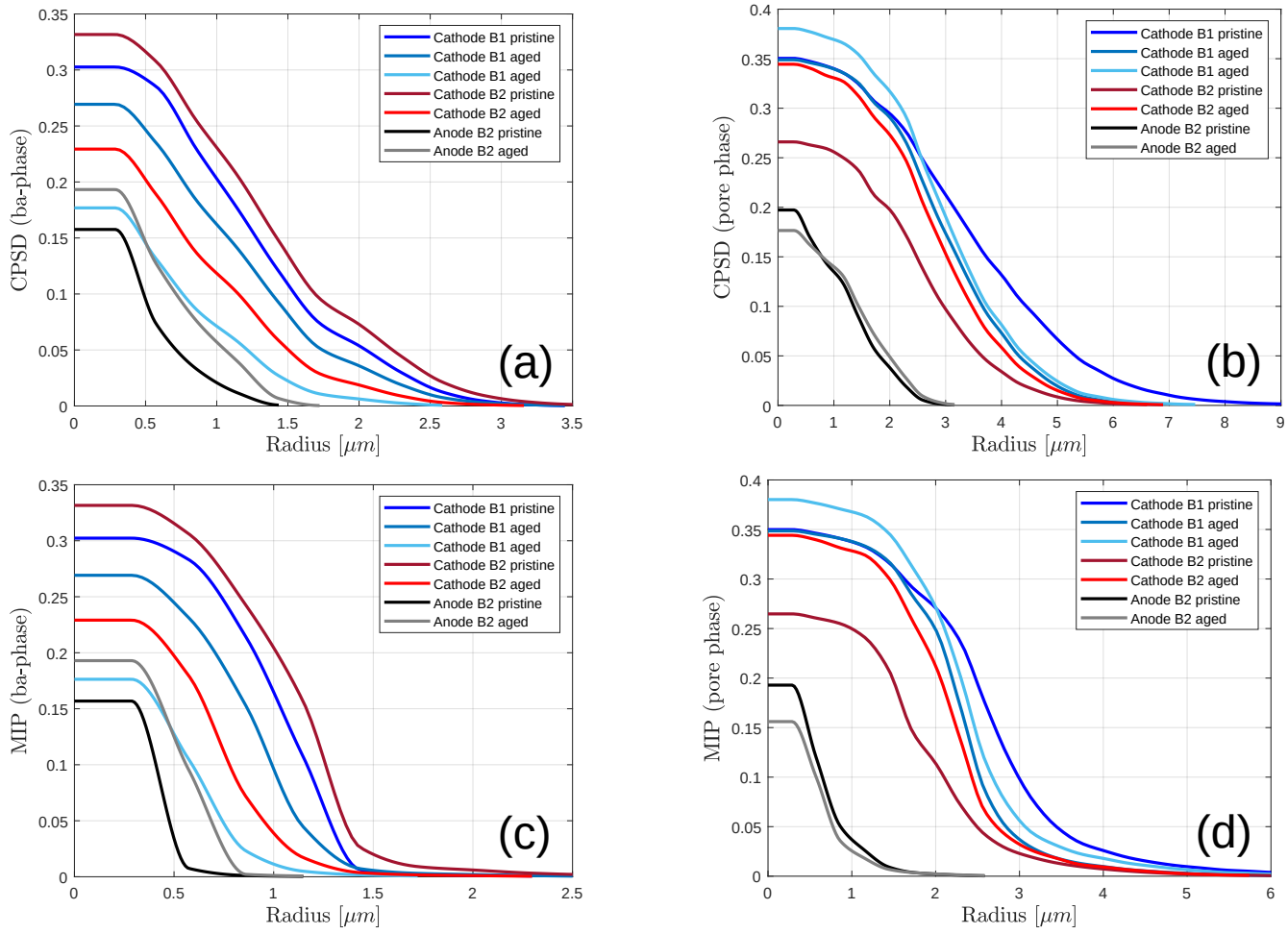


Figure 5: Continuous phase size distribution (a,b) and simulated mercury intrusion porosimetry (c,d) of the ba-phase (a,c) and the pore space (b,d) for each electrode.

reaction speed. The opposite effect on the conductivities is expected for SEI formation as the SEI's ionic conductivity but electrical insulation properties increase ionic transport but reduce electrical transport.

After having discussed CPSD and MIP, we are now able to consider the constrictivity $\beta \in [0, 1]$, which is a measure for the strength of bottlenecks, where values of $\beta$ close to one correspond to almost no constrictions [77, 70]. More formally, the notion of constrictivity is defined by $\beta = (\frac{r_{min}}{r_{max}})^2$, where $r_{min}$ and $r_{max}$ are directly computed from CPSD and MIP, respectively. More

precisely, $r_{max}$ is given by the radius for which the normalized CPSD reaches 50%, i.e., it is possible to cover half of the volume of the predefined phase with overlapping balls of radius $r_{max}$ such that the union of these balls does not intersect with the complementary phase. Analogously, $r_{min}$ can be obtained from the MIP. Figure 6a shows the results with respect to the pore space and the ba-phase. Regarding the pore space as well as the ba-phase, one can conclude that bottlenecks become more pronounced due to aging with respect to anodes, where the decreased constrictivity of the pore space indicates hindered ionic transport. Furthermore, one can observe that the constrictivity of the pore space in the cathodes slightly increases during aging, which is counterintuitive since one would expect declined transport properties as a result of cyclic aging. The constrictivity of the ba-phase decreases significantly during aging for the cathodes. This is consistent with changes in the other considered quantities and may be caused by pressure as already discussed earlier. The changes in the evaluated data imply that the aging phenomena on the anode are far more important for the transport processes than the ones at the cathode. The fact that the aging phenomena like SEI creation are mostly found at the anode is widely accepted in literature, see e.g. [66].

In the present study the constrictivity of the pore space in the anodes is dropping during aging, indicating a blocking of pores as it can be done by lithium plating and SEI formation. This is in good accordance with the decrease of SSA and volume fraction as well as the electrochemical performance, see Section 4.

From an electrochemical point of view, it is essential that the system of active particles is completely connected. Therefore, we performed a cluster analysis by means of the Hoshen-Kopelman algorithm [57], which has already been used for image preprocessing in Section 3.1. By doing so, we can detect the largest connected active material cluster and compute its volume. By dividing this volume by the total volume of the am-phase, we obtain a meaningful quantity for characterizing the connectivity of this phase. Analogously, we can compute this characteristic with respect to the ba-phase and the pore space. The results obtained for these phases are shown in Figure 6b. For the cathodes, one can observe that the ba-phase and the pore space are completely connected. Only with regard to the am-phase, a small fraction of particles is not connected. However, this

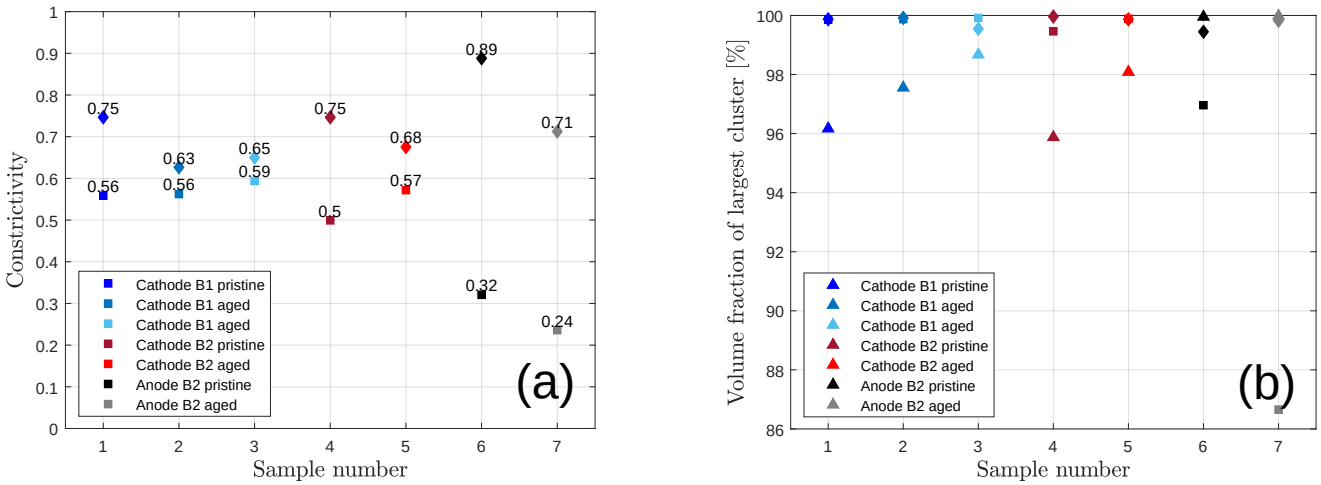


Figure 6: Constrictivity in $z$-direction of pores (squares) and ba-phase (diamonds) for each electrode (a). Volume of largest cluster divided by total volume of the considered phase (b). This characteristic is computed with respect to am-phase (triangles), ba-phase (diamonds) and pore space (squares) for each sample.

small amount of active particles is likely connected to the largest active material cluster via the ba-phase and thus contributing to the capacity of the cell. When focusing on the pristine and cyclically aged anodes, the picture becomes different since the pore space is the only phase that is not fully connected. In addition, the significant decrease in connectivity nicely coincides with the decrease of constrictivity. By combining this finding with the significant increase in geodesic tortuosity, one can conjecture that these large microstructural changes dramatically worsen the electrochemical performance.

### *3.2.2. Particle-based characteristics*

After having considered phase-based characteristics, we now deal with particle-based image characteristics, which are computed based on the particle-based segmentation described in Section 3.1.2. Note that we only considered active particles whose center of mass is contained in the sampling window, which has been used for computing the phase-based characteristics.

A first widely-used characteristic is the particle size distribution of active particles. In order to describe the size of a single active particle, we use the volume-equivalent radius. Figure 7a indicates that cyclic aging leads to a growth of graphite particles with a radius larger than two micrometer, whereas graphite particles smaller than two micrometers seem not to be affected. This leads to an increased mean particle size, see Table 3. When considering the cathode samples, one can observe only minor changes.

This results are as expected as the volume change in NCM is rather small compared to the one of graphite, which is known to increase its size by up to 13.2 percent during charging [79, 80]. The inertness of the smaller particles can not be explained for sure but may be accounted for conductive additives. They also consist of carbon and may be assigned to the am-phase but do not store lithium and therefore do not change in particle size.

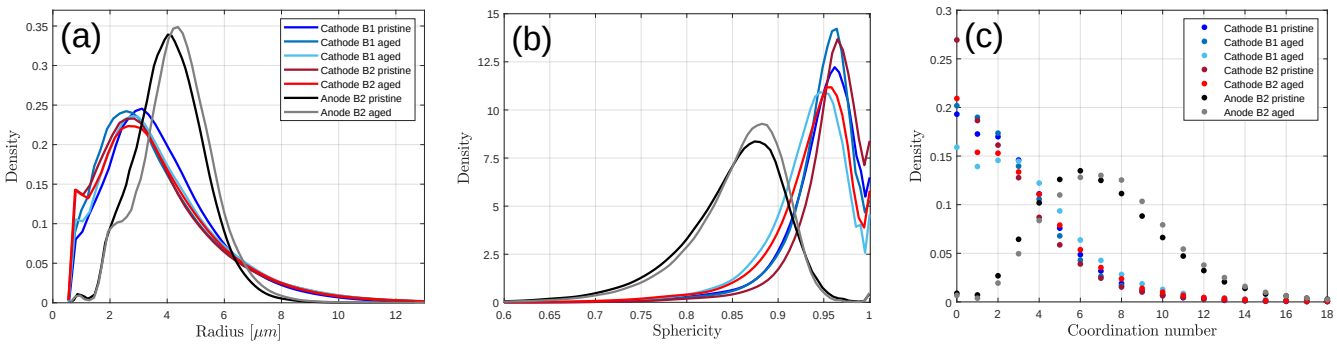


Figure 7: Distribution of particle size (a), sphericity (b) and coordination number (c) of active particles. Note that the legend of Figure 7a is also valid for Figure 7b.

After having considered the sizes of active particles, we now deal with their shapes. In order to characterize the roundness of a particle with volume $V$ and surface area $A$, we compute its sphericity defined by $\psi = \frac{\sqrt[3]{\pi}}{A}(6V)^{\frac{2}{3}}$. As it can be clearly seen in Figure 7b, the active particles in cathodes are nearly spherically shaped, whereas the graphite particles in both anodes exhibit more irregular shapes, which is in high accordance with Figure 2. Furthermore, the minor decrease

| Sample number | 1 | 2 | 3 | 4 | 5 | 6 | 7 |
|---|---|---|---|---|---|---|---|
| mean particle radius [µm] | 3.796 | 3.682 | 3.793 | 3.596 | 3.694 | 4.122 | 4.345 |
| mean sphericity [ ] | 0.951 | 0.949 | 0.934 | 0.960 | 0.940 | 0.850 | 0.856 |
| mean coordination number [ ] | 2.792 | 2.693 | 3.438 | 2.406 | 3.016 | 7.120 | 7.547 |

Table 3: Mean particle radius, mean sphericity and mean coordination number of active particles for each considered sample.

of the mean sphericity seen in Table 3 may indicate some degradation of the NCM particles of the cathodes of both batches induced by cyclic aging. This phenomenon can be explained by the loosening of small NCM particles due to mechanical stresses induced by cycling with rapid charge and discharge rates. Once again, the anodes show a contrary behavior, i.e., a slight increase of mean sphericity after aging, see Table 3. During intercalation graphite particles only grow in one direction as the graphene layers are parallel to each other and in general graphite particles show a relatively flat shape before. Therefore the particles become more spherical with intercalation of lithium.

Finally, we determined the mean coordination number, i.e., the mean number of particles that touch a given particle, where we say that two particles touch each other if there is a watershed line between those particles. Figure 7c shows a shift of the densities of coordination numbers to the right, which is also reflected by the increasing mean coordination number, see Table 3. One of the most remarkable changes with respect to cathodes is the significant reduction of unconnected NCM particles regarding batch two. Interestingly, the mean coordination number increases due to cyclic aging except for sample two. This is quite remarkable since the volume fraction of active material of sample two is about 3.5% higher compared to the corresponding pristine sample and might be explained by a more pronounced mechanical degradation.

## 4. Electrochemical measurements

Figure 8 shows the stored capacity and coulombic efficiency versus cycle number of both cells. Figure 8a corresponds to batch one electrodes, whereas Figure 8b corresponds to batch two electrodes. Both cells show a similar decrease in discharge capacity, which is relatively small if one keeps in mind the rapid rates. The charging is done mainly in the CV-phase as the fast charge rate during the CC-phase is rather inappropriate for lithium-ion storage in high energy graphite electrodes. The cell with batch one electrodes store 0.347 mAh in the 2nd cycle after formation and 0.235 mAh in the 250th cycle, which corresponds to a state of health (SOH) of around 68%. In formation cycles about 3.1 mAh at 1/5C were reached. The cell consisting of batch two electrodes shows a similar behavior since it stores 0.323 mAh in the second cycle after formation and 0.225 mAh in the 250th cycle. So about 70 percent of the initial value at that scan rate can be stored, but only a small amount compared to the formation (about 3.2 mAh at 1/5C).

The large difference of the stored capacity between the formation cycles and the rapid cycles is expected. In this work we used the same type of electrodes as in [81], which are 125 and 112 micrometer thick. Even though there is a slight difference between the batches 1 and 2, the electrode thickness is of the same order. As for example shown in [82], the electrode thickness of high energy NCM111 electrodes has a huge influence on the usable capacity of the electrodes at high C-rates. The electrodes used in this study are thicker than the thickest ones used in [82] and they suffer a great loss in available capacity above C-rates of 1C. Rapid decrease during the application of high rates is estimated. At the used high C-rates lithium plating in the high energy anode should be considered. Due to the limited diffusion rates in and into the electrodes/the covering SEI lithium can be deposited on the surface of the anode during fast charging. If this phenomenon occurs, then it depends not only on the charging rate but highly on the electrode structure. High power electrodes usually are more porous than high energy electrodes and therefore provide a larger surface area for the intake and output of lithium to store energy. Additionally, this type of electrodes is also quite thin and therefore provides short diffusion paths for the lithium ions in the electrolyte

around the electrodes. This leads to an option of using high currents to charge and discharge the battery as lithium plating is not so likely to occur due to the limited influence of the diffusion rates in the electrode and into the electrode's active material. In this work we use high energy electrodes, which are well suited to be charged at low rates, like 0.5C, but are likely to be insufficient for storing energy effectively at high rates as applied here. The low coulombic efficiency indicates side reactions like the forming of SEI on the surface of the anode or on lithium metal deposited on its surface. The SEI formation is likely to be the dominating reaction here, as the contamination of the cell components is unlikely, which would have caused a lot of side reactions in the first few cycles but not over the whole period of the cycling process. Therefore, the diffusion rates are the limiting factor as described e.g. in [83].

The low Coulomb efficiencies between 95 and 98 percent or, respectively, 96 and 99 percent during the most part of the cycling indicate irreversible side reactions such as lithium plating. Furthermore, both cells show a noticeable decrease of the specific capacity during cycling. This is in good accordance with the findings regarding the decrease of constrictivity and the increase of mean geodesic tortuosity in the anode case described in Section 3.2.1, which both indicate a decline with regard to the electrochemical performance.

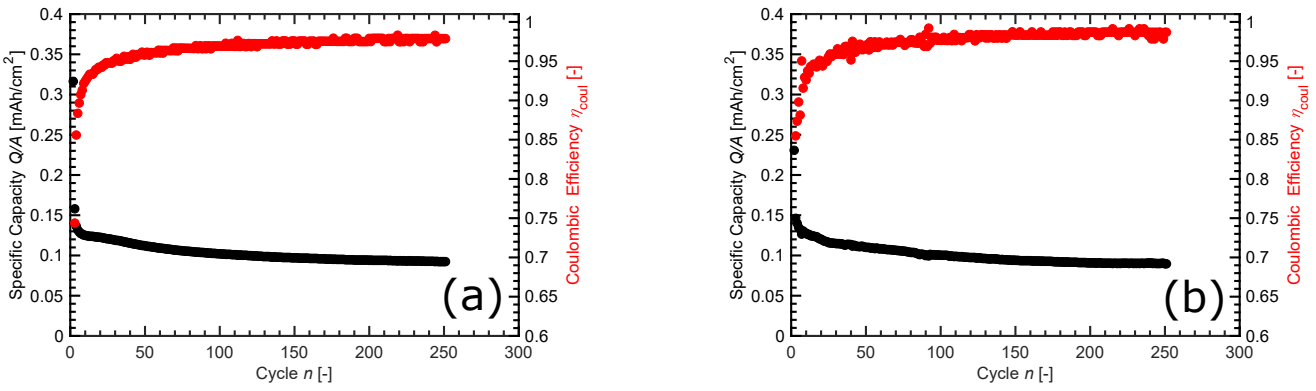


Figure 8: Specific capacity (black dots) and coulombic efficiency (red dots) versus cycle number during aging process for batch one electrodes (a) and batch two electrodes (b).

## 5. Conclusion

In this paper, three pristine and four cyclically aged electrodes have been measured by synchrotron tomography. Afterwards, a novel data-driven three-phase reconstruction approach has been applied to distinguish between active material, pores and the phase consisting of binder and conductive additive. More precisely, each voxel has been assigned to one of the three phases based on local grayscale values by means of $k$-means clustering with $k = 3$ clusters, where a post-processing step further improved the quality of the trinarization. The image processing has been completed by a particle-based segmentation by means of a marker-based watershed algorithm. Based on the preprocessed 3D image data, microstructural changes caused by cyclic aging have been quantified by means of numerous phase- and particle-based characteristics. It turned out that rapid charge and discharge rates lead to significant changes in the electrode morphology, where anodes and cathodes often show a contrary behavior. In addition, the material composition has strong influence on how pronounced the changes are in the electrode morphology due to the cyclic aging process. Furthermore, the quite different results obtained for the cyclically aged cathodes of the same batch emphasize the complex nature of aging mechanisms. This strongly indicates that rather spatially localized features than aggregated characteristics could be the driving force for severe degradation effects. Apart from the structural changes, the electrochemical performance of the cells indicates irreversible lithium loss which is likely to be caused by SEI growth and lithium plating. This coincides with the detected decrease of constrictivity as well as the significantly increased geodesic tortuosity on the anode side. To further improve the understanding of aging phenomena in lithium ion battery electrodes, we will consider a further series of anodes and cathodes in a forthcoming study, where the number of cycles and thus the strength of structural changes is varied systematically.

## Acknowledgment

This work was supported by the "Bundesministerium für Bildung und Forschung" (BMBF) through the research grants No. 05M18VUA and 05M18VSA.

We thank the beamline scientist Dr. Fabian Wilde for the technical support at the HZG P05 beamline at DESY (Hamburg, Germany).

## References

[1] B. Dunn, H. Kamath, and J.-M. Tarascaon, "Electrical energy storage for the grid: A battery of choices," *Materials for Grid Energy*, vol. 334, no. 6058, 928–935, 2011.

[2] D. Larcher and J.-M. Tarascaon, "Towards greener and more sustainable batteries for electrical energy storage," *Nature Chemistry*, vol. 7, no. 1, 19–29, 2014.

[3] B. Huang, Z. Pan, X. Su, and L. An, "Recycling of lithium-ion batteries: Recent advances and perspectives," *Journal of Power Sources*, vol. 399, 274 –286, 2018.

[4] J. Meng, Y. Suo, J. Li, G. Zheng, Y. Liu, J. Zhang, and X. Zheng, "Nitrogen-doped graphene aerogels as anode materials for lithium-ion battery: Assembly and electrochemical properties," *Materials Letters*, vol. 160, 392–396, 2015.

[5] Q. Lian, G. Zhou, X. Zeng, C. Wu, Y. Wei, C. Cui, W. Wei, L. Chen, and C. Li, "Carbon coated $SnS/SnO_2$ heterostructures wrapping on CNFs as an improved-performance anode for li-ion batteries: Lithiation-induced structural optimization upon cycling," *ACS Applied Materials & Interfaces*, vol. 8, no. 44, 30256–30263, 2016.

[6] Y. Xing, Y.-B. He, B. Li, X. Chu, H. Chen, J. Ma, H. Du, and F. Kang, "$LiFePO_4$/C composite with 3D carbon conductive network for rechargeable lithium ion batteries," *Electrochimica Acta*, vol. 109, 512–518, 2013.

[7] J. Wang, N. Yang, H. Tang, Z. Dong, Q. Jin, M. Yang, D. Kisailus, H. Zhao, Z. Tang, and D. Wang, "Accurate control of multishelled $Co_3O_4$ hollow microspheres as high-performance

anode materials in lithium-ion batteries," *Angewandte Chemie International Edition*, vol. 52, no. 25, 6417–6420, 2013.

[8] B. Wang, T. Liu, A. Liu, G. Liu, L. Wang, T. Gao, D. Wang, and X. S. Zhao, "A hierarchical porous $C$@$LiFePo_4$/carbon nanotubes microsphere composite for high-rate lithium-ion batteries: Combined experimental and theoretical study," *Advanced Energy Materials*, vol. 6, no. 16, 1600426, 2016.

[9] B. Huang, Z. Pan, X. Su, and L. An, "Tin-based materials as versatile anodes for alkali (earth)-ion batteries," *Journal of Power Sources*, vol. 395, 41–59, 2018.

[10] B. Huang, G. Li, Z. Pan, X. Su, and L. An, "Enhancing high-voltage performance of $LiNi_{0.5}Co_{0.2}Mn_{0.3}O_2$ cathode material via surface modification with lithium-conductive $Li_3Fe_2(PO_4)_3$," *Journal of Alloys and Compounds*, vol. 773, 519–526, 2019.

[11] G. Li, B. Huang, Z. Pan, X. Su, Z. Shao, and L. An, "Advances in three-dimensional graphene-based materials: configurations, preparation and application in secondary metal (Li,Na,K,Mg,Al)-ion batteries," *Energy Environmental Science*, vol. 12, 2030–2053, 2019.

[12] F. Zhang, T. Geng, F. Peng, D. Zhao, N. Zhang, H. Zhang, and S. Li, "New insights for the abuse tolerance behavior of $LiMn_2O_4$ under high cut-off potential conditions," *ChemElectroChem*, vol. 6, no. 3, 731–740, 2019.

[13] E. Thomas, I. Bloom, J. Christophersen, and V. Battaglia, "Statistical methodology for predicting the life of lithium-ion cells via accelerated degradation testing," *Journal of Power Sources*, vol. 184, no. 1, 312–317, 2008.

[14] Y. Cheng, C. Lu, T. Li, and L. Tao, "Residual lifetime prediction for lithium-ion battery based on functional principal component analysis and Bayesian approach," *Energy*, vol. 90, 1983–1993, 2015.

[15] M. Hu, J. Wang, C. Fu, D. Qin, and S. Xie, "Study on cycle-life prediction model of lithium-ion battery for electric vehicles," *International Journal of Electrochemical Science*, vol. 11, no. 1, 577–589, 2016.

[16] M. Ecker, J. B. Gerschler, J. Vogel, S. Käbitz, F. Hust, P. Dechent, and D. U. Sauer, "Development of a lifetime prediction model for lithium-ion batteries based on extended accelerated aging test data," *Journal of Power Sources*, vol. 215, 248–257, 2012.

[17] A. Barré, B. Deguilhem, S. Grolleau, M. Gérard, F. Suard, and D. Riu, "A review on lithium-ion battery ageing mechanisms and estimations for automotive applications," *Journal of Power Sources*, vol. 241, 680–689, 2013.

[18] M. Broussely, P. Biensan, F. Bonhomme, P. Blanchard, S. Herreyre, K. Nechev, and R. Staniewicz, "Main aging mechanisms in li ion batteries," *Journal of Power Sources*, vol. 146, no. 1, 90–96, 2005.

[19] P. Verma, P. Maire, and P. Novák, "A review of the features and analyses of the solid electrolyte interphase in li-ion batteries," *Electrochimica Acta*, vol. 55, no. 22, 6332–6341, 2010.

[20] M. Nie, D. P. Abraham, Y. Chen, A. Bose, and B. L. Lucht, "Silicon solid electrolyte interphase (SEI) of lithium ion battery characterized by microscopy and spectroscopy," *The Journal of Physical Chemistry C*, vol. 117, no. 26, 13403–13412, 2013.

[21] S. Cho, C.-F. Chen, and P. P. Mukherjee, "Influence of microstructure on impedance response in intercalation electrodes," *Journal of The Electrochemical Society*, vol. 162, no. 7, A1202–A1214, 2015.

[22] W. Li and J. C. Currie, "Morphology effects on the electrochemical performance of $LiNi_{1-x}Co_xO_2$," *Journal of The Electrochemical Society*, vol. 144, no. 8, 2773–2779, 1997.

[23] A. H. Wiedemann, G. M. Goldin, S. A. Barnett, H. Zhu, and R. J. Kee, "Effects of three-

dimensional cathode microstructure on the performance of lithium-ion battery cathodes," *Electrochemica Acta*, vol. 88, 580–588, 2013.

[24] V. Yufit, P. Shearing, P. D. Lee, M. Wu, and N. P. Brandon, "Investigation of lithium-ion polymer battery cell failure using X-ray computed tomography," *Electrochemistry Communications*, vol. 13, no. 6, 608–610, 2011.

[25] A. S. Mussa, A. Liivat, F. Marzano, M. Klett, B. Philippe, C. Tengstedt, G. Lindbergh, K. Edström, R. W. Lindström, and P. Svens, "Fast-charging effects on ageing for energy-optimized automotive $LiNi_{1/3}Mn_{1/3}Co_{1/3}O_2$/graphite prismatic lithium-ion cells," *Journal of Power Sources*, vol. 422, 175–184, 2019.

[26] E. M. Börger, E. Jochler, J. Kaufmann, R. Ramme, A. Grimm, S. Nowak, F. M. Schappacher, U. Rodehorst, A.-C. Voigt, S. Passerini, M. Winter, and A. Börger, "Aging of ceramic coated graphitic negative and NCA positive electrodes in commercial lithium-ion battery cells - an ex-situ study of different states of health for identification and quantification of aging influencing parameters," *Journal of Energy Storage*, vol. 13, 304–312, 2017.

[27] K. Kang, Y. S. Meng, J. Bréger, C. P. Grey, and G. Ceder, "Electrodes with high power and high capacity for rechargeable lithium batteries," *Science*, vol. 311, no. 5763, 977–980, 2006.

[28] L. Serrao, Z. Chehab, Y. Guezennee, and G. Rizzoni, "An aging model of Ni-MH batteries for hybrid electric vehicles," in *2005 IEEE Vehicle Power and Propulsion Conference*, pp. 78–85, 2005.

[29] A. Haibel, F. Beckmann, T. Dose, J. Herzen, M. Ogurreck, M. Müller, and A. Schreyer, "Latest developments in microtomography and nanotomography at PETRA III," *Powder Diffraction*, vol. 25, no. 2, 161–164, 2010.

[30] A. Haibel, M. Storm, F. Beckmann, T. Dose, F. Wilde, J. Herzen, M. Müller, A. Schreyer, V. Nazmov, M. Simon, A. Last, and J. Mohr, "Micro and nano-tomography at the GKSS

imaging beamline at PETRA III," in *Developments in X-Ray Tomography VII* (S. R. Stock, ed.), vol. 7804, 2010.

[31] W. van Aarle, W. J. Palenstijn, J. Cant, E. Janssens, F. Bleichrodt, A. Dabravolski, J. D. Beenhouwer, K. J. Batenburg, and J. Sijbers, "Fast and flexible X-ray tomography using the ASTRA toolbox," *Optics Express*, vol. 24, no. 22, 25129–25147, 2016.

[32] W. van Aarle, W. J. Palenstijn, J. D. Beenhouwer, T. Altantzis, S. Bals, K. J. Batenburg, and J. Sijbers, "The ASTRA toolbox: A platform for advanced algorithm development in electron tomography," *Ultramicroscopy*, vol. 157, 35–47, 2015.

[33] P. Coupé, P. Yger, S. Prima, P. Hellier, C. Kervrann, and C. Barillot, "An optimized blockwise nonlocal means denoising filter for 3-D magnetic resonance images," *IEEE Transactions on Medical Imaging*, vol. 27, no. 4, 425–441, 2008.

[34] A. Buades, B. Coll, and J.-M. Morel, "A non-local algorithm for image denoising," in *Proceedings of the IEEE Computer Society Conference on Computer Vision and Pattern Recognition*, vol. 2, (San Diego), pp. 60–65, IEEE Computer Society, 2005.

[35] A. Gomes, I. Voiculescu, J. Jorge, B. Wyvill, and C. Galbraith, *Implicit Curves and Surfaces: Mathematics, Data Structures and Algorithms*. London: Springer, 2009.

[36] J. Landesfeind, A. Eldiven, and H. A. Gasteiger, "Influence of the binder on lithium ion battery electrode tortuosity and performance," *Journal of The Electrochemical Society*, vol. 165, no. 5, A1122–A1128, 2018.

[37] R. Morasch, J. Landesfeind, B. Suthar, and H. A. Gasteiger, "Detection of binder gradients using impedance spectroscopy and their influence on the tortuosity of Li-ion battery graphite electrodes," *Journal of The Electrochemical Society*, vol. 165, no. 14, A3459–A3467, 2018.

[38] R. Dominko, M. Gaberscek, J. Drofenik, M. Bele, S. Pejovnik, and J. Jamnik, "The role of

carbon black distribution in cathodes for Li ion batteries," *Journal of Power Sources*, vol. 119–121, 770–773, 2003.

[39] T. Hutzenlaub, A. Asthana, J. Becker, D. Wheeler, R. Zengerle, and S. Thiele, "FIB/SEM-based calculation of tortuosity in a porous $LiCoO_2$ cathode for a Li-ion battery," *Electrochemistry Communications*, vol. 27, 77–80, 2013.

[40] M. Ender, J. Joos, T. Carraro, and E. Ivers-Tiffée, "Three-dimensional reconstruction of a composite cathode for lithium-ion cells," *Electrochemistry Communications*, vol. 13, no. 2, 166–168, 2011.

[41] M. Ender, J. Joos, T. Carraro, and E. Ivers-Tiffée, "Quantitative characterization of $LiFePO_4$ cathodes reconstructed by FIB/SEM tomography," *Journal of The Electrochemical Society*, vol. 159, no. 7, A972–A980, 2012.

[42] J. R. Wilson, J. S. Cronin, S. A. Barnett, and S. J. Harris, "Measurement of three-dimensional microstructure in a $LiCoO_2$ positive electrode," *Journal of Power Sources*, vol. 196, no. 7, 3443–3447, 2011.

[43] P. Shearing, L. Howard, P. Jørgensen, N. Brandon, and S. Harris, "Characterization of the 3-dimensional microstructure of a graphite negative electrode from a Li-ion battery," *Electrochemistry Communications*, vol. 12, no. 3, 374–377, 2010.

[44] M. Ebner, F. Marone, M. Stampanoni, and V. Wood, "Visualization and quantification of electrochemical and mechanical degradation in Li ion batteries," *Science*, vol. 342, no. 6159, 716–720, 2013.

[45] M. Ebner, F. Geldmacher, F. Marone, M. Stampanoni, and V. Wood, "X-ray tomography of porous, transition metal oxide based lithium ion battery electrodes," *Advanced Energy Materials*, vol. 3, no. 7, 845–850, 2013.

[46] B. Yan, C. Lim, L. Yin, and L. Zhu, "Three dimensional simulation of galvanostatic discharge of $LiCoO_2$ cathode based on X-ray nano-CT images," *Journal of The Electrochemical Society*, vol. 159, no. 10, A1604–A1614, 2012.

[47] S. Cooper, D. Eastwood, J. Gelb, G. Damblanc, D. Brett, R. Bradley, P. Withers, P. Lee, A. Marquis, N. Brandon, and P. Shearing, "Image based modelling of microstructural heterogeneity in $LiFePO_4$ electrodes for Li-ion batteries," *Journal of Power Sources*, vol. 247, 1033–1039, 2014.

[48] K. Kuchler, B. Prifling, D. Schmidt, H. Markötter, I. Manke, T. Bernthaler, V. Knoblauch, and V. Schmidt, "Analysis of the 3D microstructure of experimental cathode films for lithium-ion batteries under increasing compaction," *Journal of Microscopy*, vol. 272, no. 2, 96–110, 2018.

[49] L. Zielke, T. Hutzenlaub, D. R. Wheeler, I. Manke, T. Arlt, N. Paust, R. Zengerle, and S. Thiele, "A combination of X-ray tomography and carbon binder modeling: Reconstructing the three phases of $LiCoO_2$ Li-ion battery cathodes," *Advanced Energy Materials*, vol. 4, no. 8, 1301617, 2014.

[50] B. L. Trembacki, D. R. Noble, V. E. Brunini, M. E. Ferraro, and S. A. Roberts, "Mesoscale effective property simulations incorporating conductive binder," *Journal of the Electrochemical Society*, vol. 164, no. 11, E3613–E3626, 2017.

[51] A. K. Jain, "Data clustering: 50 years beyond K-means," *Pattern Recognition Letters*, vol. 31, no. 8, 651–666, 2010.

[52] G. McLachlan and D. Peel, *Finite Mixture Models*. Hoboken, NJ: J. Wiley & Sons, 2000.

[53] A. Dempster, N. Laird, and D. B. Rubin, "Maximum likelihood from incomplete data via the EM algorithm," *Journal of the Royal Statistical Society. Series B (Methodological)*, vol. 39, no. 1, 1–38, 1977.

[54] C. F. J. Wu, "On the convergence properties of the EM algorithm," *The Annals of Statistics*, vol. 11, no. 1, 95–103, 1983.

[55] G. Gan, C. Ma, and J. Wu, *Data Clustering: Theory, Algorithms, and Applications*. ASA-SIAM Series on Statistics and Applied Probability, Philadelphia, PA: Society for Industrial and Applied Mathematics, 2007.

[56] M. E. Celebi, H. A. Kingravi, and P. A. Vela, "A comparative study of efficient initialization methods for the k-means clustering algorithm," *Expert Systems with Applications*, vol. 40, no. 1, 200–210, 2013.

[57] J. Hoshen and R. Kopelman, "Percolation and cluster distribution. I. Cluster multiple labeling technique and critical concentration algorithm," *Physical Review B*, vol. 14, no. 8, 3438–3445, 1976.

[58] P. Soille, *Morphological Image Analysis: Principles and Applications*. New York: Springer, 2nd ed., 2003.

[59] L. Zielke, T. Hutzenlaub, D. R. Wheeler, C.-W. Chao, I. Manke, A. Hilger, N. Paust, R. Zengerle, and S. Thiele, "Three-phase multiscale modeling of a $LiCoO_2$ cathode: Combining the advantages of FIB-SEM imaging and X-ray tomography," *Advanced Energy Materials*, vol. 5, no. 5, 1401612, 2015.

[60] S. R. Daemi, C. Tan, T. Volkenandt, S. J. Cooper, A. Palacios-Padros, J. Cookson, D. J. L. Brett, and P. R. Shearing, "Visualizing the carbon binder phase of battery electrodes in three dimensions," *ACS Applied Energy Materials*, vol. 1, no. 8, 3702–3710, 2018.

[61] S. Vierrath, L. Zielke, R. Moroni, A. Mondon, D. R. Wheeler, R. Zengerle, and S. Thiele, "Morphology of nanoporous carbon-binder domains in Li-ion batteries–a FIB-SEM study," *Electrochemistry Communications*, vol. 60, 176–179, 2015.

[62] S. Beucher and F. Meyer, "The morphological approach to segmentation: the watershed transformation," in *Mathematical Morphology in Image Processing* (E. R. Dougherty, ed.), pp. 433–481, New York: Marcel Dekker Inc., 1993.

[63] A. Spettl, R. Wimmer, T. Werz, M. Heinze, S. Odenbach, C. Krill III, and V. Schmidt, "Stochastic 3D modeling of Ostwald ripening at ultra-high volume fractions of the coarsening phase," *Modelling and Simulation in Materials Science and Engineering*, vol. 23, no. 6, 2015. 065001.

[64] K. Kuchler, W. Westhoff, J. Feinauer, T. Mitsch, I. Manke, and V. Schmidt, "Stochastic model for the 3D microstructure of pristine and cyclically aged cathodes in Li-ion batteries," *Modelling and Simulation in Materials Science and Engineering*, vol. 26, no. 3, 2018. 035005.

[65] L. Najman and H. Talbot, *Mathematical Morphology: From Theory to Applications*. ISTE, Hoboken, NJ: Wiley, 2010.

[66] J. Vetter, P. Novák, M. Wagner, C. Veit, K.-C. Möller, J. Besenhard, M. Winter, M. Wohlfahrt-Mehrens, C. Vogler, and A. Hammouche, "Ageing mechanisms in lithium-ion batteries," *Journal of Power Sources*, vol. 147, no. 1, 269–281, 2005.

[67] K. Schladitz, J. Ohser, and W. Nagel, "Measuring intrinsic volumes in digital 3D images," in *13th International Conference Discrete Geometry for Computer Imagery* (A. Kuba, L. Nyúl, and K. Palágyi, eds.), pp. 247–258, Springer, 2007.

[68] M. Winter, K.-C. Moeller, and J. O. Besenhard, "Carbonaceous and Graphitic Anodes," in *Lithium Batteries Science and Technology* (G.-A. Nazri and G. Pistoia, eds.), pp. 145–194, Dordrecht: Kluwer Academic, 2003.

[69] Q. Liu, C. Du, B. Shen, P. Zuo, X. Cheng, Y. Ma, G. Yin, and Y. Gao, "Understanding undesirable anode lithium plating issues in lithium-ion batteries," *RSC Advances*, vol. 6, no. 91, 88683–88700, 2016.

[70] O. Stenzel, O. M. Pecho, L. Holzer, M. Neumann, and V. Schmidt, "Predicting effective conductivities based on geometric microstructure characteristics," *AIChE Journal*, vol. 62, no. 5, 1834–1843, 2016.

[71] M. B. Clennell, "Tortuosity: a guide through the maze," *Geological Society, London, Special Publications*, vol. 122, no. 1, 299–344, 1997.

[72] B. Tjaden, D. J. L. Brett, and P. R. Shearing, "Tortuosity in electrochemical devices: a review of calculation approaches," *International Materials Reviews*, vol. 63, no. 2, 47–67, 2018.

[73] D. Jungnickel, *Graphs, Networks and Algorithms*. Berlin: Springer, 3rd ed., 2008.

[74] S. Frisco, A. Kumar, J. F. Whitacre, and S. Litster, "Understanding Li-Ion Battery Anode Degradation and Pore Morphological Changes through Nano-Resolution X-ray Computed Tomography," *Journal of The Electrochemical Society*, vol. 163, no. 13, A2636–A2640, 2016.

[75] D. Aurbach, B. Markovsky, I. Weissman, E. Levi, and Y. Ein-Eli, "On the correlation between surface chemistry and performance of graphite negative electrodes for li ion batteries," *Electrochimica Acta*, vol. 45, no. 1, 67–86, 1999.

[76] B. Münch and L. Holzer, "Contradicting geometrical concepts in pore size analysis attained with electron microscopy and mercury intrusion," *Journal of the American Ceramic Society*, vol. 91, no. 12, 4059–4067, 2008.

[77] L. Holzer, D. Wiedenmann, B. Münch, L. Keller, M. Prestat, P. Gasser, I. Robertson, and B. Grobéty, "The influence of constrictivity on the effective transport properties of porous layers in electrolysis and fuel cells," *Journal of Materials Science*, vol. 48, no. 7, 2934–2952, 2013.

[78] P. Pietsch and V. Wood, "X-ray tomography for lithium ion battery research: A practical guide," *Annual Review of Materials Research*, vol. 471229, no. 1, 1–12, 2017.

[79] S. Schweidler, L. de Biasi, A. Schiele, P. Hartmann, T. Brezesinski, and J. Janek, "Volume changes of graphite anodes revisited: A combined operando X-ray diffraction and in situ pressure analysis study," *The Journal of Physical Chemistry C*, vol. 122, no. 16, 8829–8835, 2018.

[80] T. Ohzuku, Y. Iwakoshi, and K. Sawai, "Formation of lithium-graphite intercalation compounds in nonaqueous electrolytes and their application as a negative electrode for a lithium ion (shuttlecock) cell," *Journal of The Electrochemical Society*, vol. 140, no. 9, 2490–2498, 1993.

[81] A. U. Schmid, L. Lindel, and K. P. Birke, "Capacitive effects in $Li_{1-x}Ni_{0.3}Co_{0.3}Mn_{0.3}O_2 - Li_xC_y$ li-ion cells," *Journal of Energy Storage*, vol. 18, 72–83, 2018.

[82] H. Zheng, J. Li, X. Song, G. Liu, and V. S. Battaglia, "A comprehensive understanding of electrode thickness effects on the electrochemical performances of li-ion battery cathodes," *Electrochimica Acta*, vol. 71, 258–265, 2012.

[83] S. Zhang, K. Xu, and T. Jow, "Charge and discharge characteristics of a commercial $LiCoO_2$-based 18650 Li-ion battery," *Journal of Power Sources*, vol. 160, no. 2, 1403–1409, 2006.